

Investigating hydraulic loads on a crossbar block ramp using two different computational fluid dynamics models and a physical validation model

Philipp M. Helmer¹, David C. Gisen², Roman B. Weichert³

Abstract

Crossbar block ramps provide bed stability and facilitate ecological connectivity in rivers. Two major sources of uncertainty in determining their design loads are their massively turbulent flow and backwater influence.

Here, they were addressed using two computational fluid dynamics (CFD) models (created with OpenFOAM) of a complete crossbar block ramp by recording loads (forces and moments) on single crossbars. To model turbulence, the first model used the Reynolds-averaged Navier-Stokes (RANS) approach, and the second model used Large Eddy Simulation (LES). The flow in both models was transient and the free surface was tracked. Their mesh was identical and consisted of about 30.3 million cells distributed on 480 processor cores. The computed sampling interval was 180 s. The CFD models were tested against measurements of water level and pressure from a physical model. All models were in the same scale, 1: $\frac{20}{3}$. Three discharges representing three typical flow regimes were studied in each model.

Characteristics of the flow regimes were reproduced in all models. The RANS model was up to 5.3 times faster, but produced excessive waves, which likely caused over- and underestimation of crossbar loads. The LES model showed good agreement to the physical model and could be used for load predictions. However, a longer sampling interval as well as a larger variety of discharges would be required to obtain stochastically reliable estimations for the maximum loads. Both models indicated that unsteady waves in the wake-interference flow regime must be considered to find critical loads. The results can support decisions on the methods for future investigations of hydraulic loads on crossbar block ramps.

Keywords

Crossbar block ramp, Flow regime, CFD, RANS, LES, Physical model

¹philipp.m.helmer@gmail.com, Bundesanstalt für Wasserbau, Karlsruhe, Germany (until 09/2022)


²david.gisen@baw.de, Bundesanstalt für Wasserbau, Karlsruhe, Germany

³roman.weichert@baw.de, Bundesanstalt für Wasserbau, Karlsruhe, Germany

This paper was submitted on 28 October 2022. It was accepted after double-blind review on 18 April 2023 and published online on 09 May 2023.

DOI: <https://doi.org/10.48438/jchs.2023.0023>

Cite as: “Helmer, Philipp M.; Gisen, David C.; Weichert, Roman B. Investigating hydraulic loads on a crossbar block ramp using two different computational fluid dynamics models and a physical validation model. *Journal of Coastal and Hydraulic Structures*, 3. <https://doi.org/10.48438/jchs.2023.0023>”

The *Journal of Coastal and Hydraulic Structures* is a community-based, free, and open access journal for the dissemination of high-quality knowledge on the engineering science of coastal and hydraulic structures. This paper has been written and reviewed with care. However, the authors and the journal do not accept any liability which might arise from use of its contents. Copyright ©2023 by the authors. This journal paper is published under a CC-BY-4.0 license, which allows anyone to redistribute, mix and adapt, as long as credit is given to the authors. 

1 Introduction

Step-pool structures are typical bed features in steep natural streams (Montgomery and Buffington 1997; Weichert 2006). They are characterized by a sequence of bar structures running approximately crosswise to the main flow direction, with pool-like depressions between them. Artificial structures mimicking step-pool structures are widely used to provide bed stability and to facilitate ecological connectivity (Thomas et al. 2000; Maxwell and Papanicolou 2001; Maager et al. 2022; Zhang et al. 2023). They can be implemented in rivers ranging from flat lowland streams up to steep mountainous creeks and are known by different names, including step-pool ramp (Sindelar and Smart 2016) and crossbar block ramp (Oertel and Schlenkhoff 2012). The latter term is adopted in this work. Crossbar block ramps show some similarities to stepped spillways (e.g. Boes and Hager 2003), stepped cascades (e.g. Chanson 1994), square bars and ribs (e.g. Coleman et al. 2007; Singh et al. 2018; McSherry et al. 2018; Zhang and Li 2020), and cross beams in drainage channels (e.g. Fernandes de Carvalho and Lorena 2012), but differ e.g. in purpose, steepness, and emergence of flow regimes.

Three flow regimes are usually identified on crossbar block ramps (Peterson and Mohanty 1960; Morris 1968; Sindelar 2011; Oertel and Schlenkhoff 2012; Sindelar and Smart 2016). Here, in order of increasing discharge, they are referred to as *isolated roughness flow* (flow regime R1), *wake-interference flow* (R2), and *skimming flow* (R3) (Morris 1955). Their definitions vary between investigations (e.g. Ead et al. 2004) as the transition is sensitive even to marginal changes in the conditions. Qualitatively, *isolated roughness flow* is characterized by small standing waves or hydraulic jumps in the pool, which do not interact with the downstream crossbar. The energy introduced is largely dissipated within the pool, rendering the hydraulic conditions in all pools and at all crossbars similar. *Wake-interference flow* is characterized by steady to strongly unsteady waves. The unsteady waves regularly collapse and rebuild, leading to short-lived/incomplete hydraulic jumps and air entrainment. In *skimming flow*, the water level is the highest and follows the average bed slope. The main flow runs above the crossbar tops. In the pools, steady eddy structures form, which have little mass and momentum exchange with the main flow (McSherry et al. 2018).

Bed-forming flows can stabilize natural step-pool structures by creating a geometry that provides maximum flow resistance and maximum bed stability (Abrahams et al. 1995; Weichert et al. 2008). Therefore, it is reasonable to expect that interaction between geometry and flow regime plays an essential role for stability also for crossbar block ramps. In a recent study, Sindelar and Smart measured the pressure distribution around a single boulder of a block ramp in a physical model (Sindelar and Smart 2016). Their results suggest (a) that the regime change from R1 to R2 is associated with critical hydraulic conditions and (b) that the mean drag force acting on a single boulder (or crossbar) is not a good criterion to predict stability and the instantaneous drag force is required instead. The latter finding is in line with results from Zhang et al. (2022), who carried out 3D simulations of a step-pool unit and highlighted the nonuniform distribution of turbulence kinetic energy (TKE) at the crossbar and within the pool.

Existing approaches for crossbar design are based either on static equilibrium of a boulder (DWA 2014; Oertel 2015; DIN 1054) or on shear stress (Maxwell and Papanicolou 2001; Korecky and Hengl 2008). As the underlying crossbar configurations differ and the critical discharge is defined differently, they cannot be readily compared. The resulting boulder dimensions may vary significantly between approaches, depending on the boundary conditions (e.g. Hengl and Stephan 2022).

Another challenge for crossbar design is that hydraulic conditions do not only vary between flow regimes, but also along the ramp length. Many studies focused on the middle section of the ramp to exclude boundary effects from the head- and tailwater (e.g. McSherry et al. 2018; Volkart 1972). In the first and second pool, Sindelar (2011) observed particularly high bottom stresses. Effects of backwater in the most downstream section are little investigated.

To improve identification of critical flow conditions and maximum crossbar loads (e.g., moments) under consideration of backwater, a systematic study spanning a wide range of geometries, slopes, and hydraulic scenarios on a complete crossbar block ramp would be necessary. Generally, computational fluid dynamics (CFD) models are preferable for large parameter studies, as they require less effort than physical models in terms of model construction and data sampling. However, due to the massively turbulent flow on crossbar block ramps, it is not clear how to trade off computation time versus accuracy. Two common approaches to model turbulence are Reynolds-averaged Navier-Stokes (RANS, which is faster) and Large Eddy Simulation (LES, which is more accurate). Previous CFD investigations of free surface flows over complete crossbar block ramps exclusively used RANS (e.g. Premstaller 2006; Li et al. 2022; Oertel and Schlenkhoff 2012; Baki et al. 2020). More computationally intensive studies using LES as well as particle-based methods

were limited to crossbar-basin segments or segments without free water surface (Zhang and Li 2020; McSherry et al. 2018; Jalalabadi and Stoesser 2022; Xu and Jin 2014). A study comparing both CFD approaches on a complete crossbar block ramp, supported by physical validation data, is lacking.

In this paper, the above challenges are addressed by developing two unsteady CFD models using RANS and LES and evaluating them based on point measurements from a physical model with twelve crossbars in three flow regimes. The objectives are (i) to determine the hydraulic accuracy of the two CFD model approaches depending on the flow regime and streamwise position, (ii) to analyze hydraulic mechanisms causing the largest crossbar loads in the CFD models, and (iii) to quantify and to evaluate differences in the CFD crossbar load predictions. The results can support decisions on the methods for future investigations of hydraulic loads on crossbar block ramps.

2 Methods

2.1 Model geometry and boundary conditions

The geometry of the crossbar block ramp considered here is largely identical for the physical and two CFD models. The ramp consists of 12 crossbars (CR1-CR12) and 11 pools (Figure 1). Its horizontal length is 7.932 m and its width (W_{CR}) is 0.151 m in a scale of $1:\frac{20}{3}$ (Froude-scaled) to match the laboratory flume dimensions. The scaling is kept for the CFD models to ensure full comparability. The bed has a constant slope of $I = 3\%$ along the ramp and no slope in the headwater and tailwater. The crossbars are sharp-edged, right-angled and span the whole model width, at uniform height. The pools and crossbars are numbered in flow direction. Crossbar and pool dimensions conform to the minimum ecological requirements of a crossbar block ramp at large German rivers (DWA 2014).

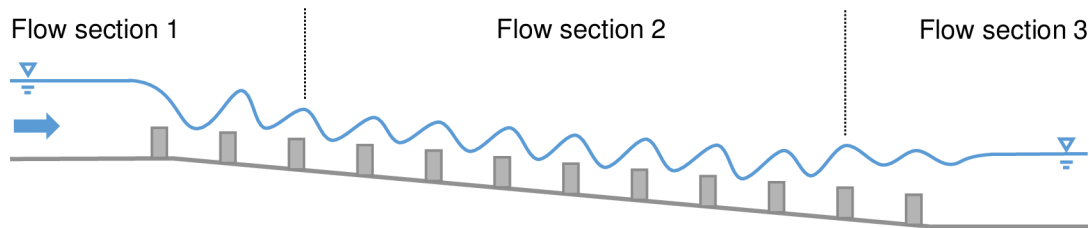


Figure 1: Schematic of the crossbar block ramp considered. Three typical flow sections can be distinguished in the water level curve (upstream-controlled, repetitive, backwater-affected). The schematic shows flow regime R2 (wake-interference flow).

A large number of parameters is expected to influence the actual flow along crossbar block ramps. The most influential are crossbar height (H_{CR}), pool length (L_P), and slope (I) (Figure 2) (Peterson and Mohanty 1960; Sindelar 2011). They are constant in crosswise direction, allowing to neglect this direction and to use a quasi-2D longitudinal section of a crossbar block ramp for the model. Crossbar openings were not considered to reduce complexity and to foster comparability. Side wall effects are negligible, as mainly non-breaking undular jumps without shock waves are expected (Ohtsu et al. 2003). Since W_{CR} is small compared to L_P , lateral flow effects are of small spatial extension and short duration. Hence, they can be considered here as negligible for the development of the primary flow (e.g. Sindelar 2011).

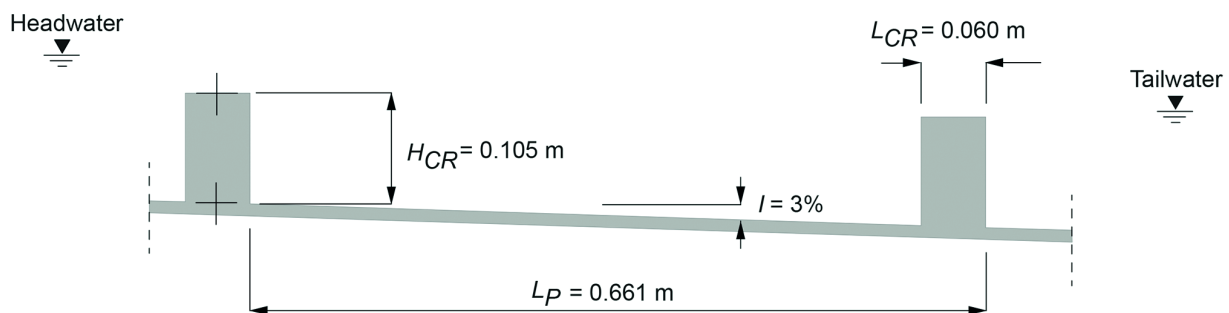


Figure 2: Longitudinal section showing design parameters and dimensions of two consecutive crossbars and their enclosed pool in model scale. H_{CR} is crossbar height, L_{CR} is crossbar length, L_P is pool length, and I is slope.

In the physical model, 17 discharges from 2.2 l/s to 56.6 l/s (Appendix A) are inspected visually. Three discharges, $Q_1 = 8.8$ l/s, $Q_2 = 17.5$ l/s, and $Q_3 = 52.6$ l/s, are gauged and chosen to elicit the three flow regimes R1-R3 (isolated roughness flow, wake-interference flow, skimming flow) and corresponding hydraulic loads in the CFD models. In real scale, they correspond to specific discharges of $q_1 = 1.0$ m³/(s·m), $q_2 = 2.0$ m³/(s·m), and $q_3 = 6.0$ m³/(s·m). Q_1 is the largest discharge still in R1, and Q_2 produced the largest waves in R2. Q_3 is the maximum technical discharge of the physical model.

Besides the flow regime, also the longitudinal position of a crossbar on the ramp is important to classify hydraulic loads. Three flow sections can be distinguished (Figure 1): the flow is either controlled by the conditions upstream of the ramp (section 1), shows repetitive hydraulics in successive pools (section 2), or is affected by backwater (section 3). This distinction was made implicitly before (e.g. Sindelar 2011; Volkart 1972; McSherry et al. 2018).

The headwater level depends on the discharge. For $Q_1/Q_2/Q_3$, it is about 0.21/0.27/0.43 m. The tailwater level is controlled in a way that the difference between headwater and tailwater is approximately 0.24 m for all discharges. Thus, both upstream and downstream water levels increase equally with increasing discharge, which is closer to real-world scenarios than a constant tailwater level.

2.2 Physical model

2.2.1 Experimental setup

The physical model is designed for pointwise validation of the CFD models. At the inlet, the flow is straightened by two honeycomb rectifiers connected in series. A movable weir controls the water level at the outlet. The distance between inlet and first crossbar is 4.45 m and the distance between last crossbar and outlet is 2.35 m. Flow rate is measured by means of magnetic induction. The maximum discharge fluctuations range around $\pm 0.9\%$ to $\pm 1.7\%$ of the target value. For construction, abrasion-resistant, non-swelling, smooth materials such as glass, plexiglass and other plastics like *Necuron* (NECUMER GmbH 2018) are used. The geometry has a maximum tolerance of approx. 1 mm.

2.2.2 Measurement technology and postprocessing

Discharge is controlled by means of an electromagnetic flow meter with an accuracy of 0.4 % (DM41F, ABB Automation 2006). Water level and pressure time-series are recorded at 10 Hz for 180 s to capture multiple periods of the waves expected in R2. Water levels are measured centrally above each crossbar (red cylinder in Figure 3a) using 12 ultrasonic probes (UP) with an accuracy of 0.15 % (UM18-212127111, SICK AG 2019). An additional UP is installed in the headwater as well as in the tailwater.

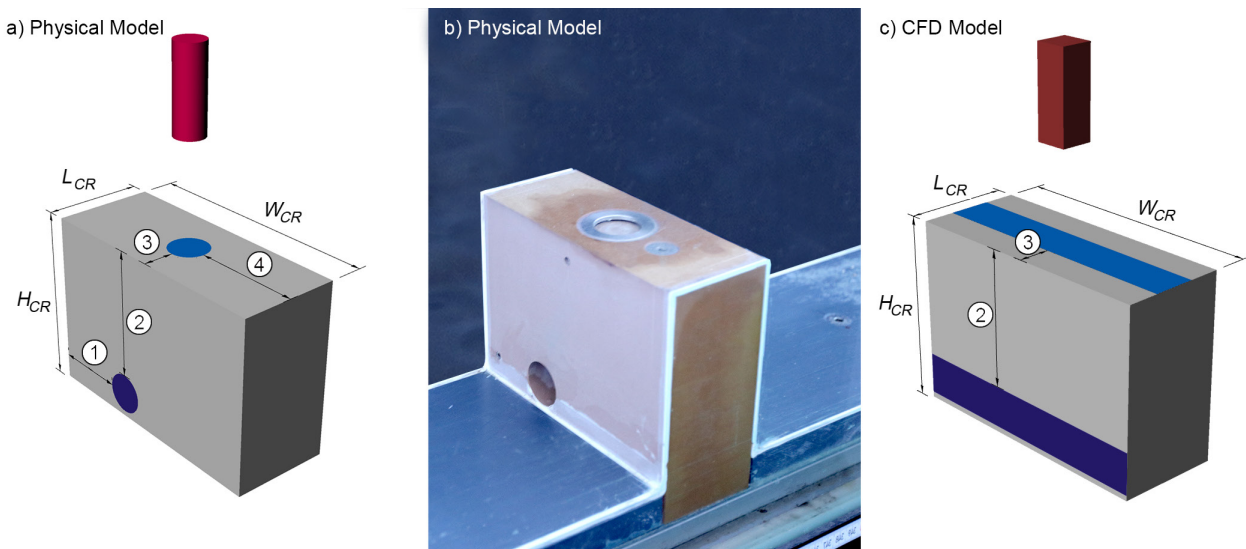


Figure 3: Measurement devices at a single crossbar in the physical and CFD model. (a) Ultrasonic probe (UP, red) and capacitive pressure transmitters CPT-Top (blue) and CPT-Bottom (purple) in the physical model, (b) photograph of the physical model, (c) numerical equivalent of UP and CPTs with larger measuring volume/zone. Viewing direction from upstream. Dimensions are ① = 40 mm, ② = 78 mm, ③ = 18 mm, ④ = 63.5 mm. Diameter of the CPT is 24 mm.

The pulse of the UP propagates in a cone shape and is reflected by the water surface. The diameter of the cone varies between 20 and 80 mm, depending on the water level. The water level position is determined from the reflection with the shortest runtime, at a point P_{ref} . As the water surface is inclined and wavy in all experiments, P_{ref} is commonly located off-center (Figure 4). In our experiments, P_{ref} can be up to 12 mm higher than the center water level. However, the measurement error relating to the center water level is smaller than that (reduced by up to 6 mm), as the UP algorithm presumes that P_{ref} is right beneath it. These effects are considered when determining the CFD comparative values.

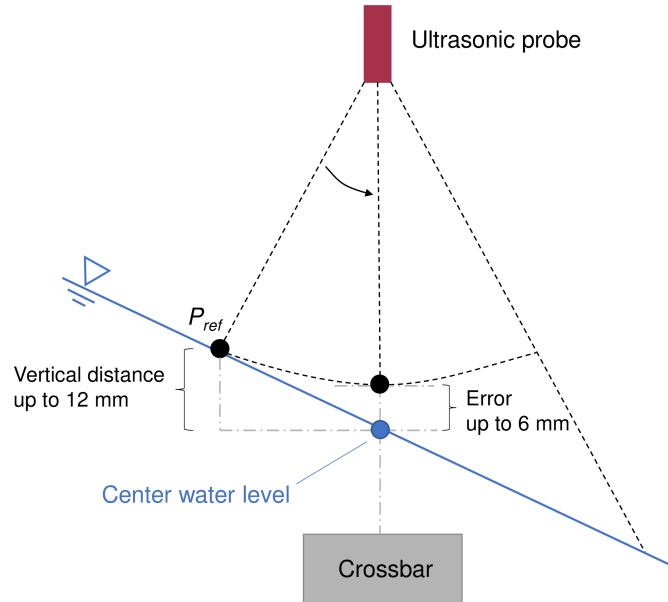


Figure 4: Example sketch of water level measurement using an ultrasonic probe (UP) with a non-horizontal water surface. Depicted is the maximum possible measurement error for the present study and the most adverse reflection point P_{ref} .

In addition, the water level between crossbars 5 and 7 is measured manually at the centerline in distances of 40 mm by means of a tip sensor. With this method, the mean water level can only be estimated, but the envelope curve can be determined reliably.

Pressure is measured using capacitive pressure transmitters (CPT) (Series 46 X, Keller AG 2021) (blue and purple circles in Figure 3a). CPTs are integrated in the top of each crossbar, where flow separation is expected to occur (CPT-Top, blue). Crossbars 1, 2, 6, 7, 11 and 12 are equipped with an additional CPT close to the bed on the upstream side, where the hydrostatic pressure is largest (CPT-Bottom, purple). The measuring area of the CPT is circular with a diameter of 24 mm, thus the measured pressure is area-averaged. Previous tests of the near-bottom pressure revealed an almost homogenous pressure field across the flume width, confirming the chosen quasi-2D model approach. Note that for Q_3 , the near-bottom pressure exceeds the measuring range of 0-300 mbar. During post-processing, a filtering algorithm is applied to remove negative water levels and significantly negative pressures.

2.3 Computational fluid dynamics models

2.3.1 Model setup

The CFD simulations are performed using the open source toolbox OpenFOAM v1812 (Heather et al. 2018). To capture the unsteady free surface and air entrainment, the multi-phase solver *interIsoFoam* (Roenby et al. 2016) is employed. It uses the *Finite Volume Method* to approximately solve the Navier-Stokes equations for incompressible fluids. The solver implements the *Volume of Fluid* method and the *IsoAdvector* scheme to sharply track the interface between water and air. Preliminary tests confirmed that *interIsoFoam* produced a sharper interface at similar computation time compared to OpenFOAM's default solver for multi-phase problems, *interFoam*.

Two CFD models are required to compare RANS- and LES-type turbulence modeling. In LES, turbulent eddies at least as large as the mesh resolution (which carry most of the turbulence energy) are resolved, and small subgrid-scale

eddies are modeled (Ferziger et al. 2020). In the standard RANS approach, generally only the mean flow is solved by the governing equations, while the influence of turbulent fluctuations is modeled (Ferziger et al. 2020; Rodi 2017). Here, unsteady RANS (URANS) is necessary to produce e.g. unsteady waves. Theoretically, its application requires that the time scale of turbulent velocity fluctuations and the time scale of slower variations in the flow (e.g. waves) differ significantly, which is unlikely here (spectral gap problem, Wilcox 2006). This is not a problem, however, as results can be tested against the physical model. For the RANS simulations, the $k-\omega$ SST turbulence model (Menter and Esch 2001) and for LES the *dynamicKEqn* turbulence model (Kim and Menon 1995) built into OpenFOAM are used. $k-\omega$ SST is one of the most popular RANS turbulence models, as it combines advantages of the $k-\varepsilon$ and $k-\omega$ models (Rodi 2017). *dynamicKEqn* uses the same boundary conditions as $k-\omega$ SST in OpenFOAM, enabling direct comparisons.

For mesh generation, OpenFOAM’s *blockMesh* and *snappyHexMesh* tools are used. The 3D model domain consists of the ramp section described in section 2.1, a 5.15 m long inlet section, and a 4.8 m long outlet section. The inlet section is designed as a submerged draft tube to avoid issues with air entrainment. The edges of the hexahedral cells run parallel to the y - and z -axis (spanwise and vertical direction, resp.). Streamwise, they are aligned with the general flow direction, i.e. with the bottom, whose slope varies within the three sections. The base resolution in $x/y/z$ - direction is $8 \times 10.1 \times 8$ mm, resp. It is coarsened in the air region away from the expected water surface and refined around the crossbars and pools, where high turbulence levels and the water surface are expected (Figure 5). The finest resolution is about $2 \times 2.5 \times 2$ mm. It is chosen according to a rule of thumb which requires to resolve at least 80 % of the turbulence kinetic energy (TKE) in the LES model. This is controlled for during postprocessing by computing the ratio of resolved to total TKE for each cell (Appendix C):

$$r_{TKE} = \frac{TKE_r}{TKE_r + TKE_{SGS}} \quad (1)$$

where TKE_{SGS} is the modeled TKE at sub-grid scales and TKE_r is the resolved TKE computed as the trace of the specific Reynolds stress tensor,

$$TKE_r = tr(\tau_{ij}) \quad (2)$$

The final mesh consists of about 30.3 million cells. It is used for both LES and RANS for full comparability, although a coarser mesh would be sufficient for RANS. For the boundary layer, results for the RANS model at Q_2 show that $y^+ \approx 20-30$ at the pool and crossbar boundaries, and $y^+ \approx 130$ at the crossbar upstream edges (Appendix D). Ideal values for use with wall functions would be $y^+ = 30-200$ so that the first cell center is well within the log layer (Wilcox 2006, p. 16). As the flow is dominated by turbulence and the ramp geometry, the influence of the boundary layer is likely negligible. Results from the physical model can help to evaluate this assumption.

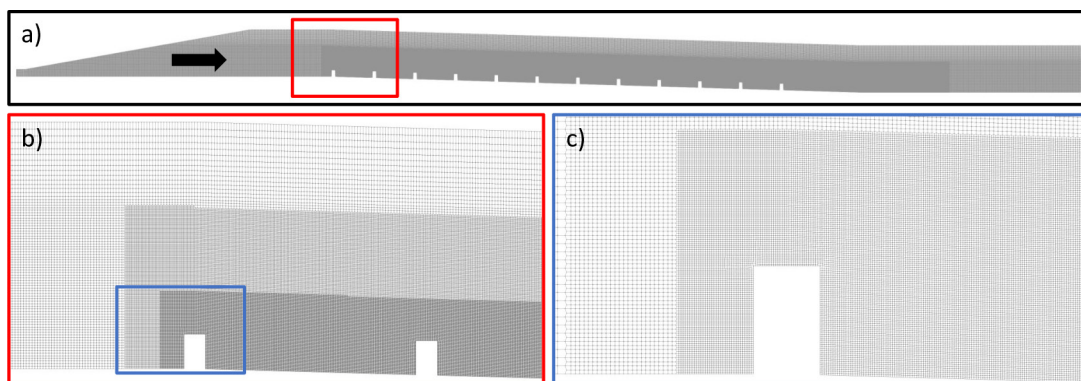


Figure 5: Longitudinal section of the computational mesh. (a) Whole crossbar block ramp with inlet and outlet sections, (b) refinement zones at crossbars 1 and 2, (c) detail of the refinement at crossbar 1.

Time is discretized using the implicit first order Euler scheme. Use of the more accurate Crank-Nicolson scheme for the LES model led to instabilities. Divergence terms are discretized by blending a higher order scheme with an upwind scheme depending on the local Courant–Friedrichs–Lewy (CFL) number. For RANS, the *limitedlinearVector* scheme is used for $CFL < 1$ and blended up to $CFL = 2$; for LES the LUST scheme (OpenCFD Ltd 2011) is used up to $CFL < 0.5$ and blended up to $CFL = 1$. In most parts of the domain, the highest CFL was ~ 0.6 .

2.3.2 Boundary conditions, initialization, processing

The inlet discharge and the outlet water level are set according to the physical model. Wall functions are applied to the walls and bed with an equivalent sand roughness of $k_s = 0.0005$ m.

Each discharge is initialized with a plane water level and a simple estimated velocity field and run in a preliminary 2D RANS model (Appendix A). After reaching a fully developed state, results are mapped to the 3D RANS model. In the same way, a fully developed 3D RANS state is mapped to the LES model. A simulation is considered fully developed (unaffected by initial conditions), when the flow rate at the inlet and outlet are approximately equal. After reaching a fully developed state, a consecutive sampling interval of 180 s is computed and analyzed in all simulations. This interval equates to the physical model interval and is currently defined by computational cost.

For each model run, 24 CPUs (Intel Xeon Gold 6138) with a total of 480 processor cores on a high-performance computer are used. Time step width varies from 10^{-3} s to 10^{-4} s, depending on the maximum flow velocity, which generally depends on the discharge. It takes between 5 and 28 days of real time to simulate the interval. For one second of simulation time, RANS requires (on average) 41/90/36 min ($Q_1/Q_2/Q_3$) and LES requires 180/220/190 min of real time. LES is thus 2.4 to 5.3 times more computationally intensive than RANS for the chosen setups. Note that the difference would be even larger if a separate, coarser mesh would have been used for RANS.

2.3.3 Postprocessing

For a pointwise comparison with the CPTs in the physical model, measurement patches are defined at the crossbars identically in both CFD models. Since the bottom pressure distribution in the physical model is approximately constant across the model width, the measurement patches can be defined as rectangles that extend over the model width. Each patch has dimensions of 151 x 24 mm (Figure 3c, blue and purple rectangles). The force acting on a patch is computed in OpenFOAM and is then divided by the patch area to obtain the mean pressure.

The numerical water surface is defined at *Volume of Fluid* parameter $\alpha.water = 0.5$. To mimic the UP measuring area in the physical model, the water level is sampled within an area of 30 x 30 mm (Figure 3c, red box) and only the maximum value is used. This approach makes it necessary to store and postprocess the complete air/water interface, limiting the measuring frequency to 2 Hz.

The CFD models also allow to compute the resultant horizontal and vertical forces acting on the whole crossbar (total flow drag and lift) and the resulting overturning moment around the base point P_{BP} (Figure 6). The sampling is performed for each crossbar with a frequency of 100 Hz.

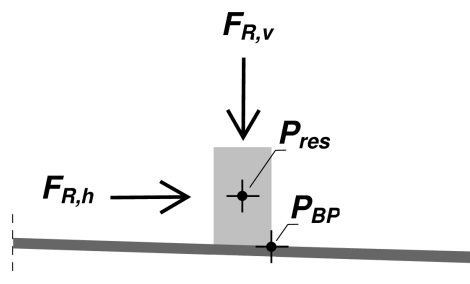


Figure 6: Resultant drag and (negative) lift forces ($F_{R,h}$ and $F_{R,v}$) acting on a crossbar. P_{res} is the point of application of the forces and P_{BP} is the base point where the moments refer to.

2.4 Accuracy and load metrics

For both accuracy and load analyses, median values of the unsteady, stochastic 180 s time series are computed as a robust measure to determine time-independent quantitative agreement or deviation. Median relative deviations between CFD and physical models are calculated as

$$\delta = \frac{\text{median}_{\{RANS, LES\}} - \text{median}_{\text{physical}}}{\text{median}_{\text{physical}}} * 100. \quad (3)$$

All pressure records (in [Pa]) are converted to pressure head (in [m]) through division by the specific weight of water (9801 kg/(m²s²) at 15 °C and 1.013 bar) to enable comparisons with the water level measurements.

The time series are summarized in boxplots, where the median value is indicated by a horizontal line inside the box. The lower and upper edge of the box mark the 25th and 75th percentile. Their difference is the interquartile range (IQR). The maximum whisker length is defined as 1.5 times the IQR. The exact whisker value corresponds to the minimum and maximum measured value within the whisker range, respectively. Outliers are represented by dots.

The IQR and outliers are used to evaluate time-dependent pressure and water level fluctuations and extreme values.

For the loads, the focus is on the outliers, as maximum values are most relevant for static-equilibrium-based design of crossbars. Also, only the overturning moment is considered and not the drag force, although both overturning and sliding are major boulder entrainment mechanisms. This is because on crossbar block ramps in lowland streams, the crossbars are usually embedded in the subsoil, so that overturning around the base point P_{BP} (Figure 6) is way more relevant than sliding. The model design neglects questions of subsoil stability and pool material dimensioning in order to focus on the hydraulic loads.

3 Results and discussion

3.1 Flow regimes

Before the 3D CFD models are used to analyze and to quantify crossbar loads (section 3.3), they are evaluated by means of the characteristic flow regimes (this section) and, quantitatively, on the basis of pointwise water level and pressure data from the quasi-2D physical model (section 3.2). Analysis takes into account the streamwise position (flow section) of the crossbars and pools.

The three discharges selected (Q_1 - Q_3) are suitable to elicit the three general flow regimes (R1-R3) in all three models, but with some interesting differences in detail. In the physical and LES model, Q_1 produces a regime in the upper end of R1, Q_2 produces a regime in the middle range of R2, and Q_3 produces a regime at the end of R2/beginning of R3 (Figure 7a, c). While Q_3 is distinctly different from Q_2 , its regime still shows minor sporadic waves and cannot be classified as a typical R3. This result illustrates the problems of a clear delineation of the regimes. The time-averaged water level of the physical model is reproduced very well in LES, including characteristic wave patterns in Q_1 and Q_2 (Figure 7a, c).

Comparing the time-averaged water level for Q_1 and Q_2 in RANS (Figure 7b), the wave peak in the pools occurs further downstream than in the physical and LES model. By definition, when wave peaks reach the downstream crossbar, the flow regime starts to change from R1 to R2. Thus, this transition begins at a lower flow rate in RANS than in the physical and LES model (this is also true for the transition between R2 and R3). As a consequence, the flow regime produced by Q_1 is closer to R2 than to R1 in RANS. For Q_2 , R2 emerges as intended, but the instantaneous water levels exhibit an increased fluctuation range, i.e. larger waves.

Evaluation of the differences between model types and the influence of flow regimes on the hydraulics and crossbar loads requires a more detailed inspection, as described in the following.

3.2 Water level and pressure head

3.2.1 Flow section 1

In general, there is a very good agreement between both CFD models and the physical model in flow section 1 (see Figure 1) for all discharges. That is because for all discharges, the water level and pressure head at crossbar 1 (Figure 8, Q_1 - Q_3 , left column) fluctuate only slightly compared to the other crossbars. The slight pulsation of the headwater level (< 1 cm) is due to a standing wave in pool 1, whose peak is slightly moving. Hydraulically, the system communicates downstream and upstream.

The absolute difference between water level (Figure 8, Q_1 - Q_3 , a-d) and pressure head at the top of all crossbars (Figure 8, Q_1 - Q_3 , e-f) is widely explained by the influence of dynamic pressure, which is not considered in the hydrostatic calculation of pressure head. For crossbar 1 (CR1), however, the difference is larger than for subsequent crossbars. This

is likely caused by a stable, large-scale detachment zone present for all discharges at the upper edge of CR1, which reduces local pressure (Figure 9a, c).

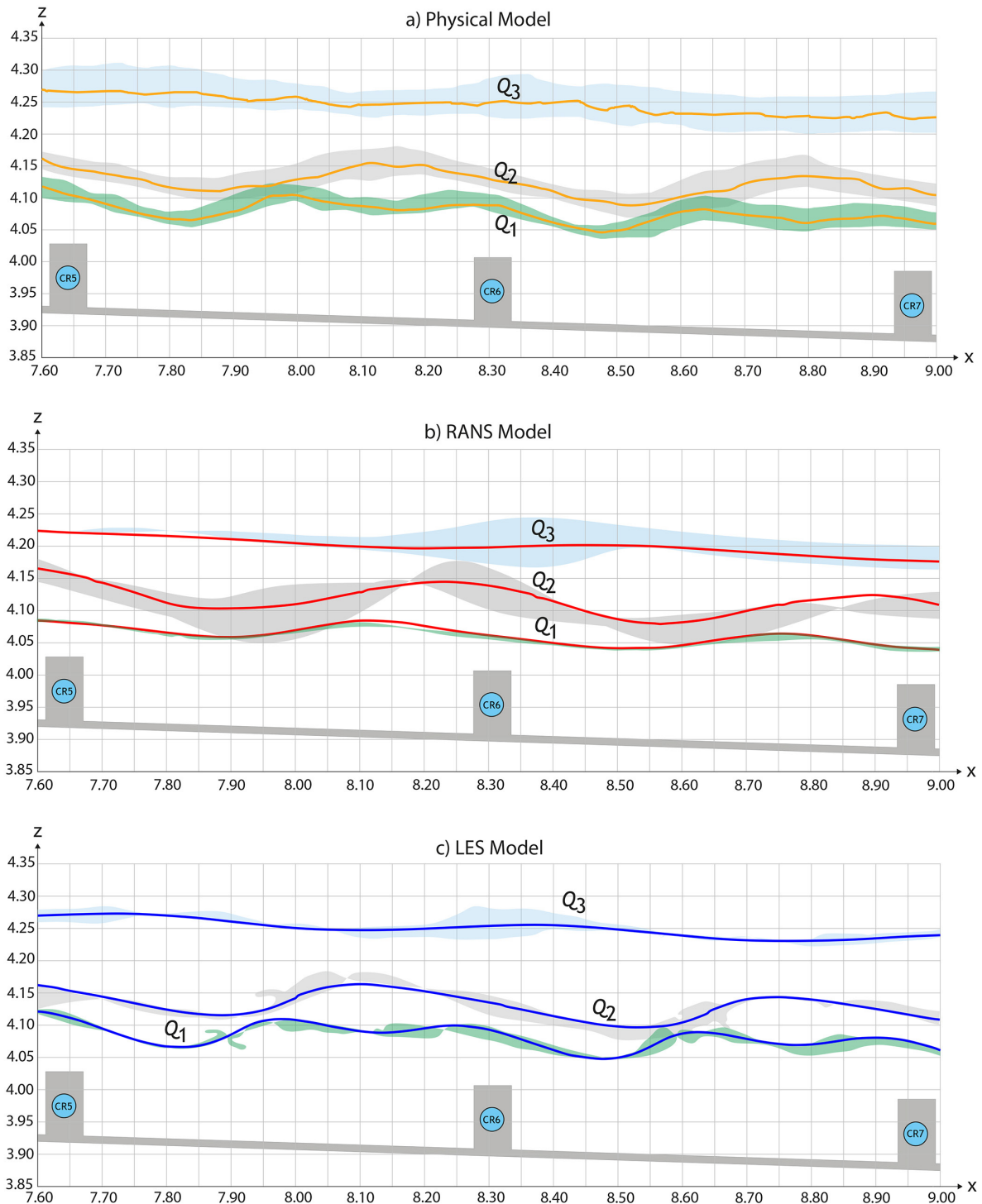


Figure 7: Centerline water level of all models and discharges (Q_1 - Q_3) for pools 5 and 6 between crossbars CR5 and CR7 in (a) physical model, (b) RANS model, (c) LES model. Thicker lines are time-averaged water levels. Green (Q_1), gray (Q_2) and blue (Q_3) areas denote the water level envelope (extreme values) for the physical model and selected instantaneous water levels for the CFD models, respectively. Axes show model coordinates in [m].

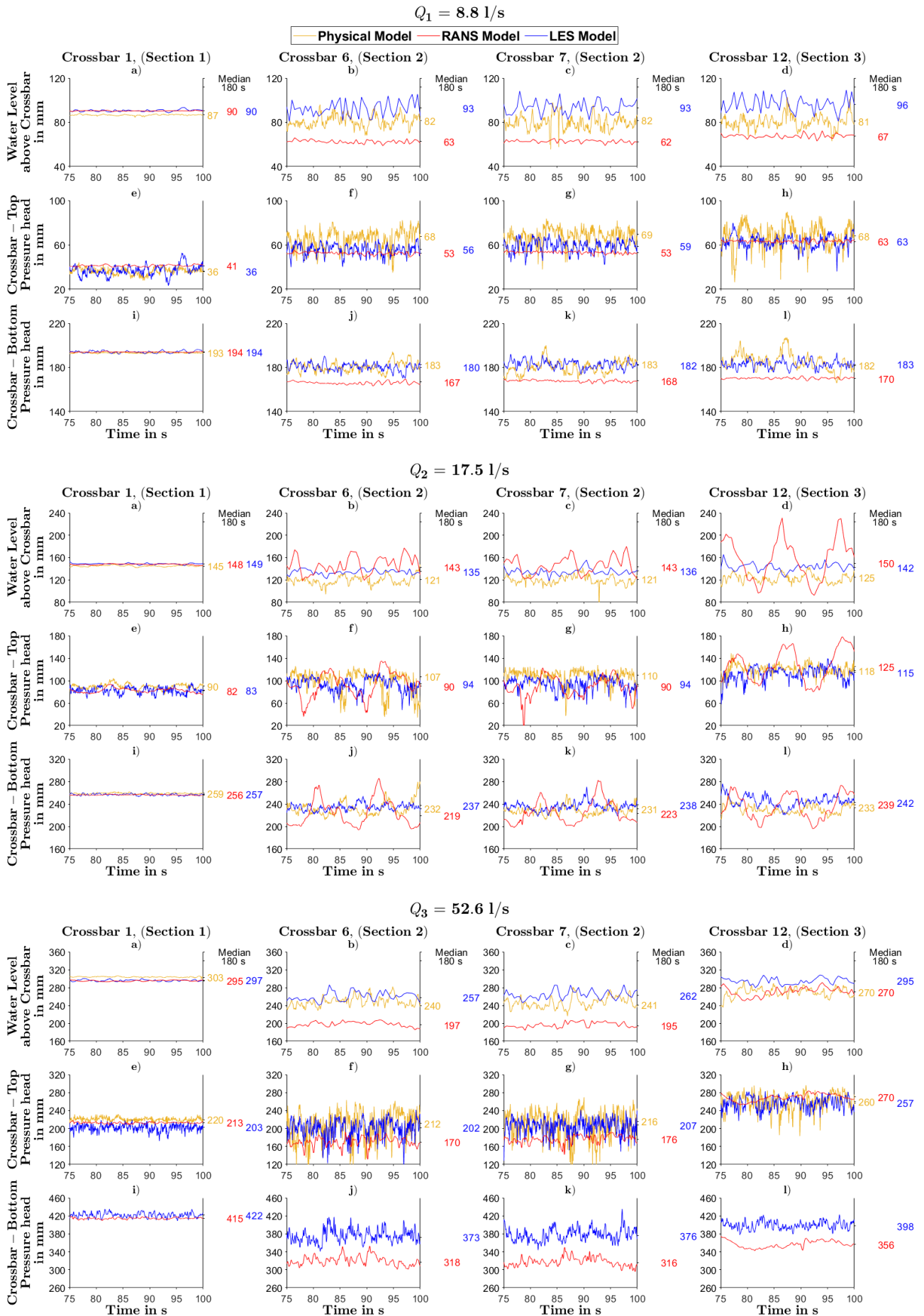


Figure 8: Time series of water level (a-d), pressure head at crossbar top (e-h) and crossbar bottom (i-l) at crossbars CR1 (section 1), CR6 and CR7 (section 2), and CR12 (section 3) for discharges Q_1 - Q_3 . Depicted is a 25-s-segment of the recorded 180-s-sampling interval for the physical and two CFD models. The median value computed over 180 seconds is denoted on the right-hand side of each subplot. The near-bottom pressure of the physical model is missing in subplot Q_3 (i-l) as it exceeded the measuring range.

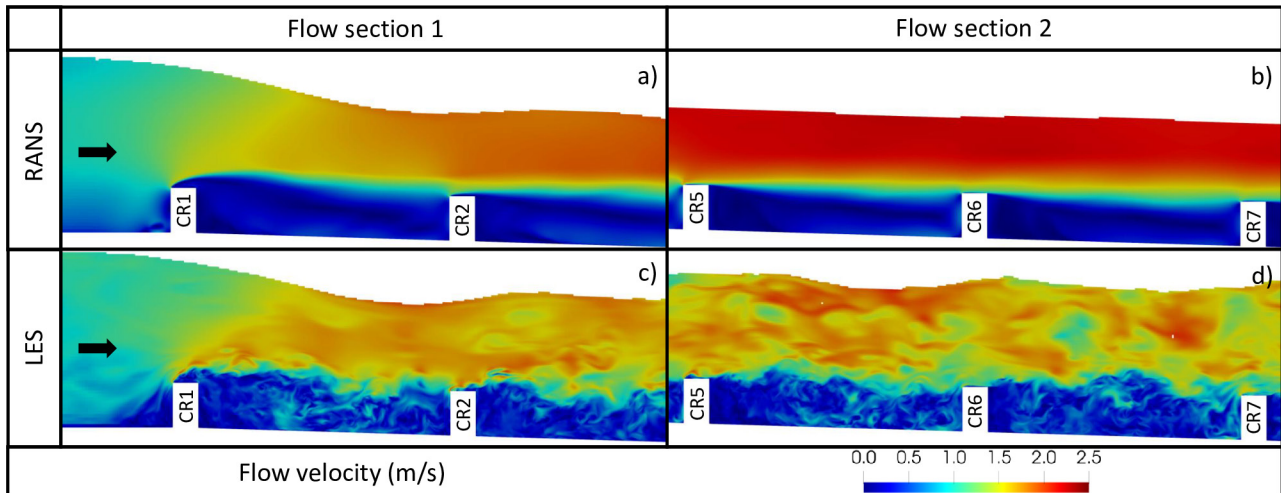


Figure 9: Instantaneous flow fields for Q_3 in the RANS-type and LES-type CFD model centerline show their principle difference in turbulence resolution. It is inherent in the unsteady RANS approach that short-term fluctuations are muted, while long-term fluctuations can be resolved. Comparing sections 1 and 2, a flow detachment at the edge of crossbar 1 (CR1) occurs in section 1, and the flow velocities are higher in section 2.

3.2.2 Flow sections 2 and 3

In sections 2 and 3, the general agreement between the LES model and physical model is good. Relative deviations of the medians are between $\delta = 1\%$ - 19% (Eq. 3, Figure 8, Q_1 - Q_3 , crossbars 6, 7, 12). The RANS model differs a bit more from the physical model in the medians ($\delta = 0\%$ - 24%). For discharge Q_2 , it exhibits strong qualitative differences. Q_2 here represents flow regime R2, which is characterized by recurring collapsing standing waves. They are produced in all three models, but have a larger period and amplitude in RANS (Figure 8, Q_2 , crossbars 6, 7, 12). The pressure head range in RANS is up to 80 mm, which is twice as large as in the other models (e.g. Figure 8, Q_2 , k). A possible explanation is that short-term velocity and pressure fluctuations, i.e. turbulence, are muted in RANS models (Figure 9). Therefore, more energy is available to build up waves with larger amplitude and longer period. Similar insufficient reproduction of unsteady, free-surface hydraulic jumps in a RANS model has been reported by Premstaller (2006).

A second systematic difference with RANS for Q_3 are constantly lower water levels (Figure 8, Q_3 , b, c) and pressure heads (Figure 8, Q_3 , f, g) in section 2 compared to the physical model. The difference can be explained by the flow regime, which corresponds to a developing flow regime R3, in which the main flow is directed above the crossbar tops (Figure 9b, d). Beneath the main flow, inside the pools, eddy structures develop, which is a well-known effect (e.g. McSherry et al. 2018). In RANS, streamlines and flow velocity in the main flow are more homogeneous than in LES and mass exchange between the main flow and pool flow is reduced. This leads to an increased main flow velocity, which, along with continuity, can explain the reduced water levels and pressure heads. In section 3, at CR12, the difference between the models is smaller, because the downstream water level is controlled by the same boundary condition for all three model types (Figure 8, Q_3 , d, h).

3.2.3 Fluctuations and maxima

To better evaluate the accuracy of maximum values predicted by the CFD models, fluctuations of water level and pressure (i.e., waves) of the full 180 s time series recorded are summarized in Figure 10.

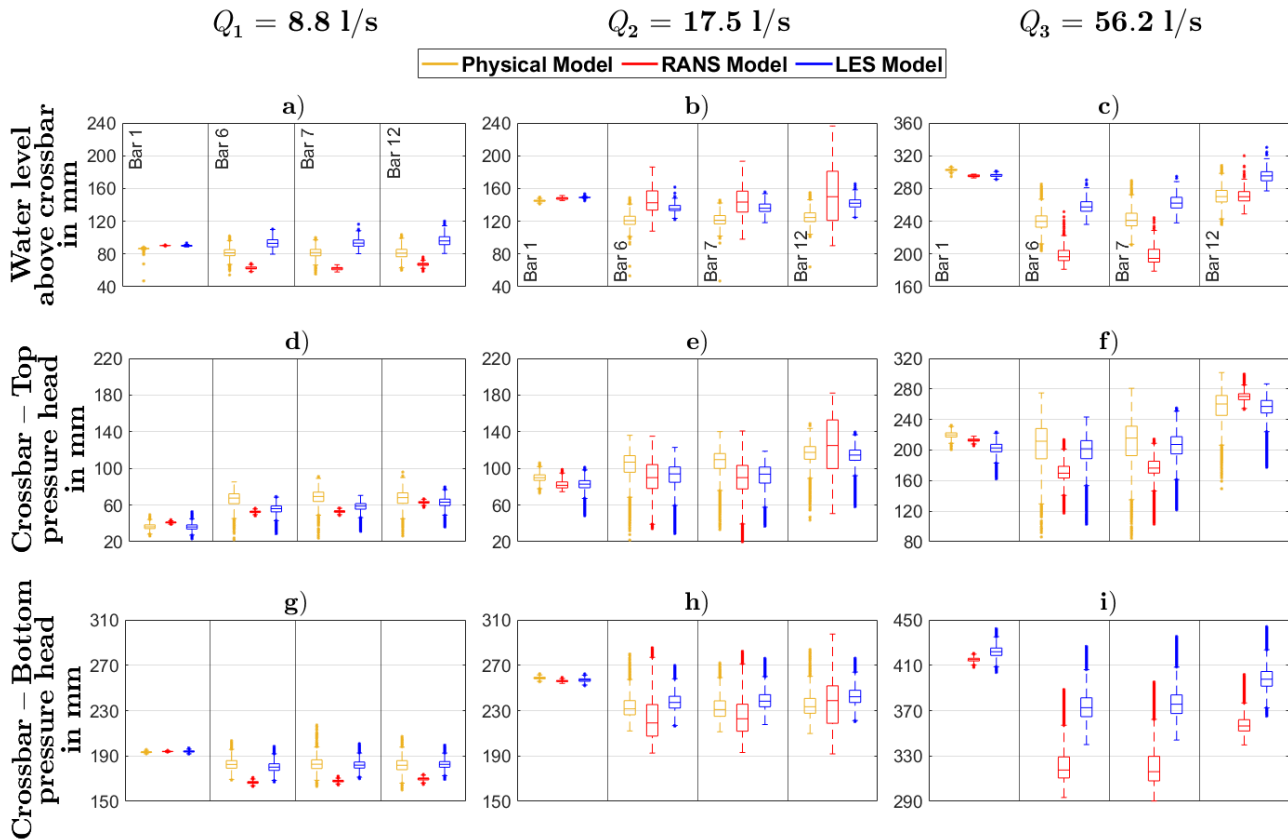


Figure 10: Boxplots summarizing water level and pressure head distributions at four selected crossbars for three discharges Q_1 - Q_3 and three model types. Note that the y-axis limits deviate. The grid line spacing is constant at 40 mm. The near-bottom pressure of the physical model is missing in subplot (i) as it exceeded the maximum measuring value.

The pressure head is not normally distributed, since outliers are negatively skewed at the crossbar top (Figure 10d-f) and positively skewed at the crossbar bottom (Figure 10g-i). This trend is present in the physical and the CFD models, indicating a qualitatively correct representation of the complex flow characteristics around the crossbars by the CFD models.

Quantitatively, water level and pressure head fluctuations (measured by the IQR) for Q_1 (Figure 10a, d, g) and Q_3 (Figure 10c, f, i) are mostly smaller in RANS compared to the physical model. For Q_2 , the RANS IQR deviates in the other direction and is a multiple of the IQR of the physical model. This can also be explained by recurring collapsing standing waves, which characterize flow regime R2, but are too high in the RANS model (section 3.2.2). As the development and collapse of waves is reflected in the pressure field at a crossbar, the dynamic maximum pressure on the crossbars is systematically overestimated for Q_2 in RANS. Preliminary 2D-RANS simulations for a larger variety of discharges (Appendix B, pressure results not shown) indicate that RANS can also exhibit systematic overestimations for other discharges in R2, where self-induced unsteady waves appear. For Q_3 , RANS underestimates water level and pressure clearly.

For LES, the water levels are slightly overestimated, but the pressure head results are in a good to very good agreement to the physical model results. The LES IQR is similar and plausible compared to the physical model at most crossbars for all discharges and sections. This is also confirmation for the assumption that it is not necessary to strictly adhere to numerical advice to keep $y^+ = 30$ -200 for this flow (section 2.3.1).

In summary, both the time-resolved and summarized results reveal some important limitations of the RANS approach for the analysis of dynamic loads on a crossbar block ramp. While RANS is able to produce reliable results at CR1 for all discharges and RANS models are sufficient for many other study objectives at ramps (e.g. Baki et al. 2017; Oertel and Schlenkhoff 2012; Premstaller 2006), unsteady LES simulations are required to produce plausible fluctuation maxima in R2 and the beginning of R3. This result could be explained by the assessment that the RANS method is generally limited for massive flow separation (Spalart 2009), which occurs at the crossbars.

However, the level of accuracy needed can vary with the objective of a study, and sometimes the speed advantage of RANS versus LES (up to 5.3 times here) could be more important. From a design perspective this would be admissible, if RANS reliably overestimated the maximum loads. This question cannot be answered using just two physical point measurements, as it is methodically unclear how they correlate to the load on an entire crossbar. Therefore, it is approached using the CFD-computed moments in the following.

3.3 Overturning moments

3.3.1 Maximum moments

Moments around the base point P_{BP} (see Figure 6) are shown in Figure 11. First, the maxima of the moments are considered, as they are most relevant for static-equilibrium-based design of crossbars. As the RANS results are not fully reliable (see discussion above), they are analyzed just qualitatively.

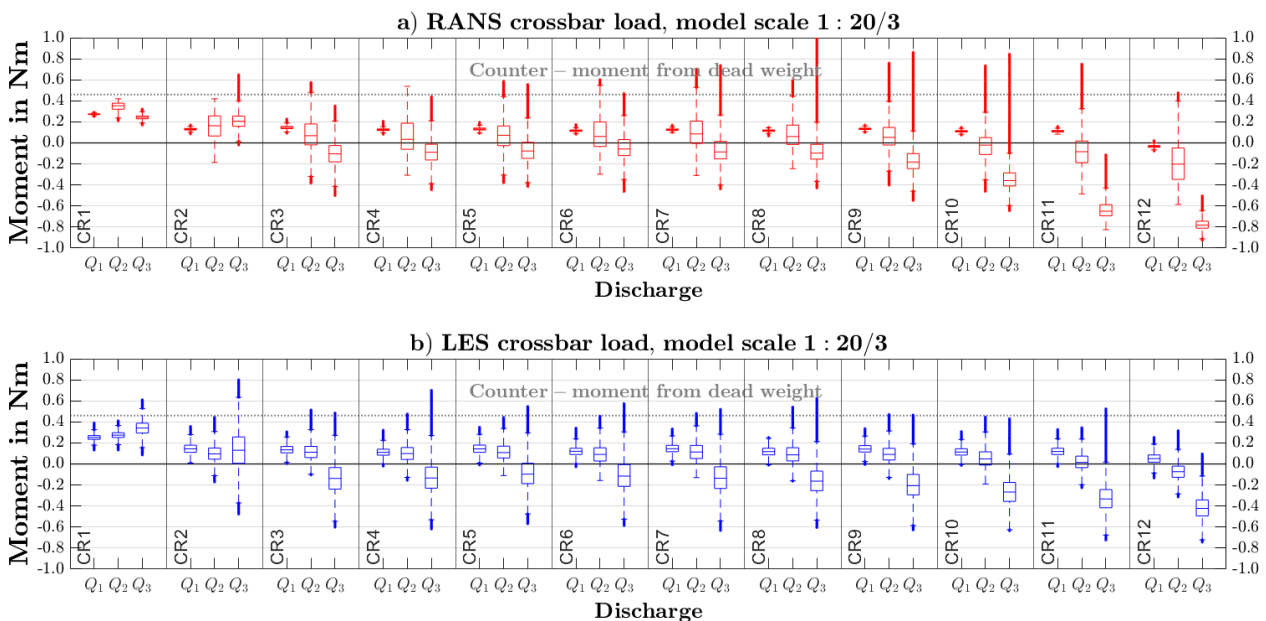


Figure 11: Boxplots of moments around the base point (P_{BP}) sampled over 180 s for all crossbars and discharges (Q_1 - Q_3) of (a) RANS and (b) LES. The dotted gray line indicates the moment that can be compensated by the dead weight of a crossbar, calculated for a block with a density of 2600 kg/m^3 placed loosely on the bottom (not embedded in the ground, dimensions see Figure 2).

The maximum moments for RANS are generally, but not always, larger than for LES. This ambiguity rules out the option to use a RANS in a parameter study to improve design, as unpredictable load underestimations are not acceptable for design processes.

Focusing on the discharges, the highest outliers are mostly in Q_3 , with the outliers in Q_2 not far below or sometimes even higher for both model types. Both results do agree well with studies reporting the critical loads in R2 (Sindelar 2011; Sindelar and Smart 2016), considering that the flow for Q_3 is between R2 and R3. Q_1 appears to be too far into R1 to reproduce distinct critical hydraulic conditions as reported by Sindelar and Smart (2016). Both findings indicate that it is necessary to inspect a variety of discharges from all over R2, including the transitions to R1 and R3, to identify maximum loads.

The large temporal variability of the moments, visible in the long whiskers and outlier range of Q_2 and especially Q_3 , gives rise to the assumption that maximum (and minimum) loads are associated with single large waves (see section 3.2.2). It is in-line with recent findings indicating that instantaneous drag forces should be preferred over mean drag forces for boulder stability (Sindelar and Smart 2016). As the simulation time of 180 s limited the number of single large waves to build up and collapse, no statistical descriptor, e.g. a confidence interval, of the maximum loads could be computed.

The gray line in Figure 11 indicating the theoretical counter-moment is exceeded multiple times. It is just informative, though, as the calculation presumes a loose block. In reality, blocks are embedded in the ground and thus can resist larger moments. Also note that dynamic pressure (and thus, horizontal force and the moment) is likely overestimated here compared to natural blocks, which are more streamlined than the rectangular blocks used in this study. Still, from the LES results it is very clear that high moments can occur all along the ramp, from CR1 to CR11. An effect of backwater on the maximum moment is only present at the deeply submerged CR12 (Figure 11b).

3.3.2 Median moments

To find general correlations between flow features and crossbar loads, the more robust median moments are considered. In both models, the median moments for Q_3 are clearly smaller than the median moments for Q_2 in absolute terms, and even negative for most of section 2 (Figure 11a, b, CR3-7). This result can be attributed to two complementary effects (see Figure 6): (i) an increase in the stabilizing vertical force $F_{R,v}$ in Q_3 , caused by the increased water column acting on the crossbar top (Figure 8, Q_1 - Q_3 , subfigures b, Zhang et al. 2022); (ii) a decrease in the overturning horizontal force $F_{R,h}$, caused by flow separation into main flow above the crossbars and eddies in the pools (text section 3.2.2). Both effects reduce the turning moment around P_{BP} . The strongly negative median moments for Q_3 indicate that the vertical force is much larger (up to ten times) than the horizontal force, i.e. on average a crossbar gets more stable with increasing discharge in R3.

With rising backwater and, thus, water column in section 3, effects (i) and (ii) are amplified and thus, the median moments are even lower compared to section 2 (Figure 11b, CR8-12). These results suggest that for increasing discharge, crossbar stability is less and less affected by the flow and higher discharges are less relevant for determining design loads (Sindelar and Smart 2016).

Finally, CR1 is exposed to the highest loads in terms of the medians for both models, at all crossbars and all discharges. There is also little difference between Q_1 - Q_3 there, which would indicate that CR1 is the most critical crossbar for design. However, the load range (IQR and outliers) at CR1 is the smallest of all crossbars (Figure 11a, b) and it is clear from the LES model that, unlike the median values, the load range increases with discharge and is largest for Q_3 . Hence, other crossbars are likely to be affected by similar or larger maximum loads.

3.3.3 Constraints

A comparison of the maximum moments found with literature values of critical moments is not feasible, as it would require so many assumptions that the result would be arbitrary. Still, the results can indicate conditions (flow regime and location) of maximum loads on a crossbar block ramp. Under the assumption that these conditions are scale-invariant and temporal dependencies can be ignored, critical loads could be expected to occur on ramps with similar dimensions (H_{CR}/L_P and I) in the same conditions.

Air entrainment could be a relevant process especially in R2, but air bubbles cannot be scaled in the models. Possible scale effects are treated as negligible compared to advection and turbulence. They do not affect comparisons between the physical and CFD models, as they are in the same scale.

4 Conclusions

Two CFD models were tested against a physical model of a quasi-2D longitudinal section of a crossbar block ramp. Three discharges (Q_1 - Q_3) related to three flow regimes (R1-R3) were analyzed in three flow sections of the ramp. The high spatial and temporal resolution of the CFD models (up to 2 mm, 0.0001 s, model scale $1:\frac{20}{3}$) ensured sufficient detail to identify agreement and deviations between physical and CFD models. Conclusions regarding the CFD accuracy are:

- Both CFD model types are able to reproduce the characteristics of the three typical flow regimes on a crossbar block ramp, i.e. they are both suitable for qualitative studies.
- Only the LES model is suitable to investigate instantaneous loads, which must be considered to find the critical loads.

- The RANS model shows large qualitative deviations for unsteady waves, i.e. increased amplitude and period. Such waves are typical for R2 as well as for pools just slightly affected by backwater (transition from flow section 2 to flow section 3) in all flow regimes. RANS-type turbulence models should be used with care in these conditions.
- LES is estimated to be up to 5.3 times more computationally intensive than RANS for the present study. The difference would be even larger if a mesh optimized for RANS would be used. LES is thus currently unsuitable for a systematic study covering a wide range of parameters.

Analysis of the loads in the CFD models revealed that:

- Overturning moments are likely highest for flow regimes which are characterized by unsteady waves, i.e. flow regime R2, but also in the transition to R3. According to this result, it is necessary to investigate a range of discharges all over R2 and into R3 to find maximum loads.
- Maximum moments do likely result from single large waves.
- Backwater only lowers the median moments; in dependence on the local water level. A reducing effect on the maximum moments is only present at deeply submerged crossbars, where the flow regime changes to R3 due to backwater.

Future work should investigate the excessive wave formation in RANS. Insights could help clarify whether the use of RANS is only permissible for steady flow conditions, or also for transient conditions. In the former case, a more advanced, but still efficient, approach should be sought. Different approaches trying to blend the speed and accuracy of RANS and LES are available, for example Detached-Eddy Simulation (DES) (Spalart 2009). Finally, quantifying the influence of backwater in conjunction with smaller slopes, different boulder shapes, gaps between boulders, fluctuating discharges, and different pool lengths in flow section 1, could further improve the efficiency of crossbar block ramp design.

Acronyms and symbols

Acronym/symbol	Description	Value and units
CFD	Computational Fluid Dynamics	
CFL	Courant–Friedrichs–Lewy (number)	
CPT-Bottom/Top	Capacitive Pressure Transmitters - at crossbar bottom (upstream facing surface) - at crossbar top (horizontal surface)	
CPU	Central Processing Unit	
CR1-CR12	Crossbar 1 to crossbar 12	
δ	Median relative deviation between CFD and physical model	
$F_{R,h}$	Resultant horizontal force (total flow drag)	
$F_{R,v}$	Resultant vertical force (total flow weight)	
H_{CR}	Middle height of a crossbar	0.105 m
I	Slope of the crossbar block ramp investigated	3%
IQR	Interquartile range	
k_s	Equivalent sand roughness	
L_{CR}	Length of a crossbar	0.060 m
L_P	Length of a pool (including L_{CR})	0.661 m
LES	Large Eddy Simulation	
LUST	Linear-Upwind Stabilized Transport	
P_{BP}	Point for determining the base point moment	
P_{res}	Point of application of the resultant force	
P_{ref}	Point at the water surface, where the measuring signal of the UP is reflected.	
Q_1 - Q_3	Discharges: $Q_1 = 8.8$ l/s $Q_2 = 17.5$ l/s $Q_3 = 52.6$ l/s	
R1-R3	Flow regimes: R1 = isolated roughness flow R2 = wake-interference flow R3 = skimming flow	

RANS	Reynolds-Averaged Navier–Stokes	
τ_{ij}	Specific Reynolds stress tensor	
TKE	Turbulence kinetic energy	
UP	Ultrasonic probe	
W_{CR}	Width of a crossbar, resp. model width	0.151 m
y^+	Dimensionless wall distance	

Acknowledgements

The authors gratefully acknowledge the contributions of Jochen Eckhardt and Volker Haushalter to the physical model. The authors also thank all members of the hydraulic laboratory and unit W1 of the Bundesanstalt für Wasserbau, Karlsruhe, Germany, for their support.

Author contributions (CRediT)

PMH¹: Conceptualization, Data curation, Formal Analysis, Investigation, Methodology, Project administration, Software, Validation, Visualization, Writing – original draft, Writing – review & editing. DCG²: Investigation, Methodology, Software, Validation, Writing – original draft, Writing – review & editing. RBW³: Conceptualization, Funding acquisition, Methodology, Resources, Supervision, Validation, Writing – review & editing.

References

- ABB Automation (2006): Electromagnetic Flowmeter Primary with Pulsed DC Magnetic Field Technology. Operating Instructions. Rev. 02/05.2006. Göttingen, Germany (D184B062U02). Available online at <https://library.abb.com/d/D184B062U02>, checked on 4/17/2023.
- Abrahams, A. D.; Li, G.; Atkinson, J. F. (1995): Step-Pool Streams: Adjustment to Maximum Flow Resistance. In *Water Resour. Res.* 31 (10), pp. 2593–2602. DOI: 10.1029/95WR01957.
- Baki, A. B. M.; Zhu, D. Z.; Harwood, A.; Lewis, A.; Healey, K. (2017): Rock-weir fishway II. Design evaluation and considerations. In *Journal of Ecohydraulics* 2 (2), pp. 142–152. DOI: 10.1080/24705357.2017.1369183.
- Baki, A. B. M.; Zhu, D. Z.; Harwood, A.; Lewis, A.; Healey, K. (2020): Hydraulic design aspects of rock-weir fishways with notch for habitat connectivity. In *Journal of Ecohydraulics* 5 (1), pp. 94–109. DOI: 10.1080/24705357.2019.1652706.
- DIN 1054, 2010: Baugrund - Sicherheitsnachweise im Erd- und Grundbau - Ergänzende Regelungen zu DIN EN 1997-1.
- Boes, R. M.; Hager, W. H. (2003): Hydraulic Design of Stepped Spillways. In *J. Hydraul. Eng.* 129 (9), pp. 671–679. DOI: 10.1061/(ASCE)0733-9429(2003)129:9(671).
- Chanson, H. (1994): Hydraulic design of stepped cascades, channels, weirs and spillways. 1. ed. Oxford u.a.: Pergamon Press.
- Coleman, S. E.; Nikora, V. I.; McLean, S. R.; Schlicke, E. (2007): Spatially Averaged Turbulent Flow over Square Ribs. In *Journal of Engineering Mechanics* 133 (2), pp. 194–204. DOI: 10.1061/(ASCE)0733-9399(2007)133:2(194).
- DWA (2014): Merkblatt DWA-M 509. Fischaufstiegsanlagen und fischpassierbare Bauwerke - Gestaltung, Bemessung, Qualitätssicherung. Edited by Deutsche Vereinigung für Wasserwirtschaft, Abwasser und Abfall e.V. (DWA). Hennef (DWA-Regelwerk).
- Ead, S. A.; Katopodis, C.; Sikora, G. J.; Rajaratnam, N. (2004): Flow regimes and structure in pool and weir fishways. In *Journal of Environmental Engineering and Science* 3 (5), pp. 379–390. DOI: 10.1139/s03-073.
- Fernandes de Carvalho, R.; Lorena, M. (2012): Roughened Channels with Cross Beams Flow Features. In *J. Irrig. Drain Eng.* 138 (8), pp. 748–756. DOI: 10.1061/(ASCE)IR.1943-4774.0000457.
- Ferziger, J. H.; Perić, M.; Street, R. L. (2020): Computational Methods for Fluid Dynamics. 4th ed. 2020. Cham: Springer (Springer eBook Collection).
- Heather, A.; Janssens, M.; Ferraris, S.; Olesen, M.; Sonakar, P.; Ghildiyal, P. et al. (2018): OpenFOAM. Version v1812: ESI Group/OpenCFD Ltd. Available online at <https://develop.openfoam.com/Development/openfoam/-/tree/OpenFOAM-v1812>, checked on 7/13/2022.

- Hengl, M.; Stephan, U. (2022): Beckenrampen - Dimensionierung und Stabilität bei Hochwasser. In *WasserWirtschaft* (4), pp. 26–32.
- Jalalabadi, R.; Stoesser, T. (2022): Reynolds and dispersive shear stress in free-surface turbulent channel flow over square bars. In *Physical review. E* 105 (3-2), p. 35102. DOI: 10.1103/PhysRevE.105.035102.
- Keller AG (2021): Kapazitiver Transmitter für Pegelmessung. Serie 46X, Serie 46X-Ei. www.keller-druck.com. Available online at <https://download.keller-druck.com/api/download/YPgBVfB4QyaekTLvs3wN3d/de/2021-11.pdf>, checked on 7/14/2022.
- Kim, W.-W.; Menon, S. (1995): A new dynamic one-equation subgrid-scale model for large eddy simulations. In AIAA (Ed.): 33rd Aerospace Sciences Meeting and Exhibit, vol. 33. Reno, NV, U.S.A. Available online at <https://arc.aiaa.org/doi/10.2514/6.1995-356>, checked on 7/18/2022.
- Korecky, N.; Hengl, M. (2008): Stabilität und Bemessung von flach geneigten, aufgelösten Riegelrampen. In *Wasserwirtsch* 98 (1-2), pp. 32–36. DOI: 10.1007/BF03241451.
- Li, S.; Yang, J.; Ansell, A. (2022): Evaluation of Pool-Type Fish Passage with Labyrinth Weirs. In *Sustainability* 14 (3), p. 1098. DOI: 10.3390/su14031098.
- Maager, F.; Hohermuth, B.; Weitbrecht, V.; Boes, R. (2022): Effect of Discharge Variations and Sediment Supply on the Stability of Artificial Step-Pool Sequences. In Miguel Ortega-Sánchez (Ed.): Proceedings. 39th IAHR World Congress - From Snow to Sea. Granada, Spain, 19.06.2022 - 24.06.2022: International Association for Hydro-Environment Engineering and Research (IAHR), pp. 1135–1144.
- Maxwell, A. R.; Papanicolou, A. N. (2001): Step-pool morphology in high-gradient streams. In *International Journal of Sediment Research* 16 (3), pp. 380–390.
- McSherry, R.; Chua, K.; Stoesser, T.; Mulahasan, S. (2018): Free surface flow over square bars at intermediate relative submergence. In *Journal of Hydraulic Research* 56 (6), pp. 825–843. DOI: 10.1080/00221686.2017.1413601.
- Menter, F. R.; Esch, T. (2001): Elements of Industrial Heat Transfer Predictions. In COBEM (Ed.): Proceedings. Invited Lectures - Engineering for the New Millenium. 16th Brazilian Congress of Mechanical Engineering – COBEM. Uberlândia, 26.-30.11.2001 (20), pp. 117–127.
- Montgomery, D. R.; Buffington, J. M. (1997): Channel-reach morphology in mountain drainage basins. In *Geological Society of America Bulletin* 109 (5), pp. 596–611. DOI: 10.1130/0016-7606(1997)109%3C0596:CRMIMD%3E2.3.CO;2.
- Morris, H. M. (1955): Flow in Rough Conduits. In *Transactions of the American Society of Civil Engineers* 120, pp. 373–398. DOI: 10.1061/TACEAT.0007206.
- Morris, H. M. (1968): Hydraulics of Energy Dissipation in Steep, Rough Channels (Research Division bulletin, 19).
- NECUMER GmbH (2018): NECURON® 100. Blockmaterial - Technisches Datenblatt. www.necumer.de. Available online at http://www.necumer.com/images/pdf/de/NECURON_100_db.pdf, checked on 7/14/2022.
- Oertel, M. (2015): Bemessung von Blocksteinrampen in Riegelbauweise – Hydraulik und Stabilität. In *WasserWirtschaft* 105 (7/8), pp. 51–56.
- Oertel, M.; Schlenkhoff, A. (2012): Crossbar Block Ramps. Flow Regimes, Energy Dissipation, Friction Factors, and Drag Forces. In *J. Hydraul. Eng.* 138 (5), pp. 440–448. DOI: 10.1061/(ASCE)HY.1943-7900.0000522.
- Ohtsu, I.; Yasuda, Y.; Gotoh, H. (2003): Flow Conditions of Undular Hydraulic Jumps in Horizontal Rectangular Channels. In *J. Hydraul. Eng.* 129 (12), pp. 948–955. DOI: 10.1061/(ASCE)0733-9429(2003)129:12(948).
- OpenCFD Ltd (2011): OpenFOAM 2.1.0 - release notes. Numerical Methods. Available online at <https://openfoam.org/release/2-1-0/numerics-multiphase-mules/>, checked on 7/18/2022.
- Peterson, D. F.; Mohanty, P. K. (1960): Flume Studies of Flow in Steep, Rough Channels. In *J. Hydr. Div.* 86 (9), pp. 55–76. DOI: 10.1061/JYCEAJ.0000543.
- Premstaller, G. (2006): Hybrid Investigation of Wave Formation in Steep, Stepped Channels. Dissertation. Leopold-Franzens-University of Innsbruck.
- Rodi, W. (2017): Turbulence Modeling and Simulation in Hydraulics: A Historical Review. In *J. Hydraul. Eng.* 143 (5), Article 03117001. DOI: 10.1061/(ASCE)HY.1943-7900.0001288.
- Roenby, J.; Bredmose, H.; Jasak, H. (2016): A computational method for sharp interface advection. In *Royal Society Open Science* 3 (11). Available online at <https://doi.org/10.1098/rsos.160405>, checked on 7/13/2022.

- SICK AG (2019): Ultraschallsensoren. UM30, UM18, UM12, UC30, UC12, UC4, UD18. Available online at https://cdn.sick.com/media/docs/9/09/709/product_information_ultrasonic_sensors_um30_um18_um12_uc30_uc12_uc4_ud18_de_im0043709.pdf, checked on 7/14/2022.
- Sindelar, C. (2011): Design of a Meandering Ramp. TU Graz. Institut für Wasserbau und Wasserwirtschaft. Available online at <https://graz.pure.elsevier.com/en/publications/design-of-a-meandering-ramp>, checked on 7/15/2022.
- Sindelar, C.; Smart, G. (2016): Transition Flow in Step-Pool Systems. Pressure Distributions and Drag Forces. In *J. Hydraul. Eng.* 142 (10), p. 4016035. DOI: 10.1061/(ASCE)HY.1943-7900.0001165.
- Singh, S. K.; Raushan, P. K.; Debnath, K.; Mazumder, B. S. (2018): Turbulent oscillatory flow along unidirectional current over square ribs. In *Can. J. Civ. Eng.* 45 (4), pp. 248–262. DOI: 10.1139/cjce-2017-0337.
- Spalart, P. R. (2009): Detached-Eddy Simulation. In *Annu. Rev. Fluid Mech.* 41 (1), pp. 181–202. DOI: 10.1146/annurev.fluid.010908.165130.
- Thomas, D. B.; Abt, S. R.; Mussetter, R. A.; Harvey, M. D. (2000): A Design Procedure for Sizing Step-Pool Structures. In Rollin H. Hotchkiss, Michael Glade (Eds.): Building Partnerships. Joint Conference on Water Resource Engineering and Water Resources Planning and Management. Minneapolis, Minnesota, United States, July 30-August 2, 2000. Reston, VA: American Society of Civil Engineers, pp. 1–10.
- Volkart, P. (1972): Die Stabilisierung von Flussläufen mittels einer Folge von Querschwellen. Edited by Prof. Dr. D. Vischer. Eidgenössische Technische Hochschule Zürich (Mitteilungen der Versuchsanstalt für Wasserbau, Hydrologie und Glaziologie, 6).
- Weichert, R. (2006): Bed Morphology and Stability of Steep Open Channels. Edited by Prof. Dr.-Ing. H.-E. Minor. Eidgenössische Technische Hochschule Zürich (Mitteilungen der Versuchsanstalt für Wasserbau, Hydrologie und Glaziologie, 192). Available online at <https://www.research-collection.ethz.ch/handle/20.500.11850/1797>, checked on 7/22/2022.
- Weichert, R. B.; Bezzola, G. R.; Minor, H.-E. (2008): Bed morphology and generation of step-pool channels. In *Earth Surf. Process. Landforms* 33 (11), pp. 1678–1692. DOI: 10.1002/esp.1639.
- Wilcox, D. C. (2006): Turbulence Modeling for CFD. 3rd ed. La Cañada, California: DCW Industries, Inc.
- Xu, T.; Jin, Y.-C. (2014): Numerical investigation of flow in pool-and-weir fishways using a meshless particle method. In *Journal of Hydraulic Research* 52 (6), pp. 849–861. DOI: 10.1080/00221686.2014.948501.
- Zhang, C.; Hassan, M. A.; Saletti, M.; Zimmermann, A. E.; Xu, M.; Wang, Z. (2023): A Unit-Scale Framework for Designing Step-Pool Sequences. In *J. Hydraul. Eng.* 149 (1), Article 04022033, p. 4022033. DOI: 10.1061/(ASCE)HY.1943-7900.0002033.
- Zhang, C.; Xu, Y.; Hassan, M. A.; Xu, M.; He, P. (2022): A combined approach of experimental and numerical modeling for 3D hydraulic features of a step-pool unit. In *Earth Surf. Dynam.* 10 (6), pp. 1253–1272. DOI: 10.5194/esurf-10-1253-2022.
- Zhang, Z.; Li, S. S. (2020): Large Eddy Simulation of Near-Bed Flow and Turbulence over Roughness Elements in the Shallow Open-Channel. In *Water* 12 (10), p. 2701. DOI: 10.3390/w12102701.

Appendix A

Table A-1: Discharges inspected visually in the physical model. Cases 4, 7, and 17 are used in the 3D CFD models.

No.	Discharge (l/s)	Specific discharge q [m ³ /(m·s)]
	Model scale 1:20/3	Real scale 1:1
1	2.2	0.25
2	4.4	0.50
3	6.6	0.75
4	8.8	1.00
5	12.3	1.40
6	14.9	1.70
7	17.5	2.00
8	19.7	2.25
9	21.9	2.50
10	24.1	2.75
11	26.3	3.00
12	30.7	3.50
13	35.1	4.00
14	39.5	4.50
15	43.9	5.00
16	48.2	5.50
17	52.6	6.00

Appendix B

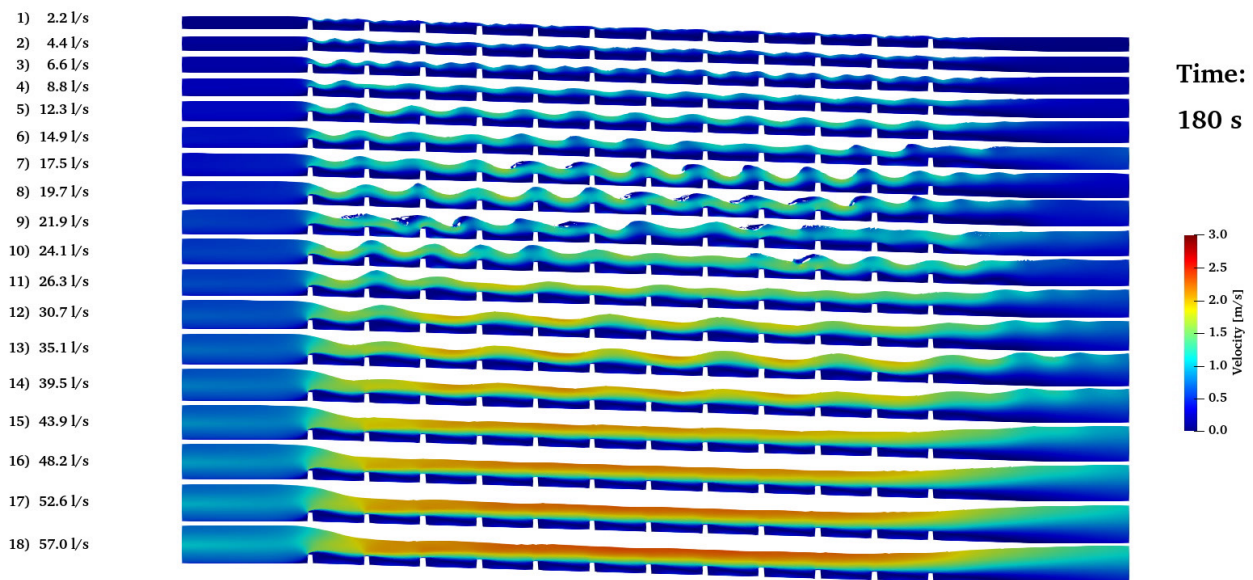
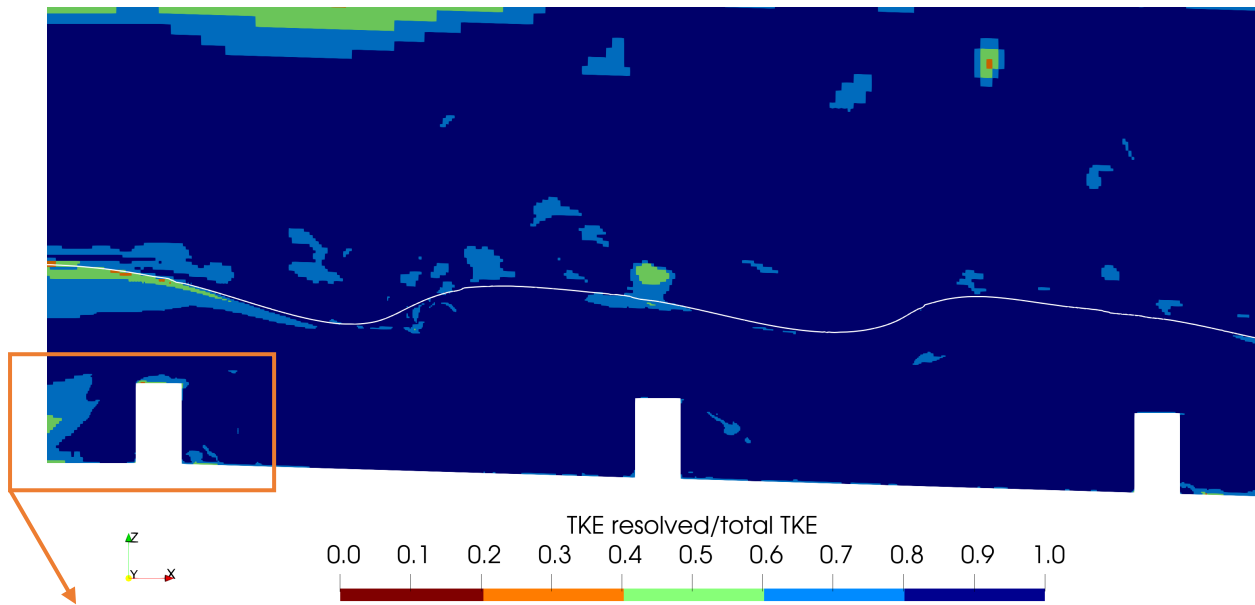


Figure B-1: Instantaneous streamwise cross-sections showing 18 discharges computed in a preliminary 2D RANS model, scale 1:20/3. For discharges, see also Table 1. A rough attribution to flow regimes would categorize cases 1-3 in R1, cases 4-13 in R2, and cases 15-18 in R3, but is not transferable to the other models.

Appendix C

(a)



(b)

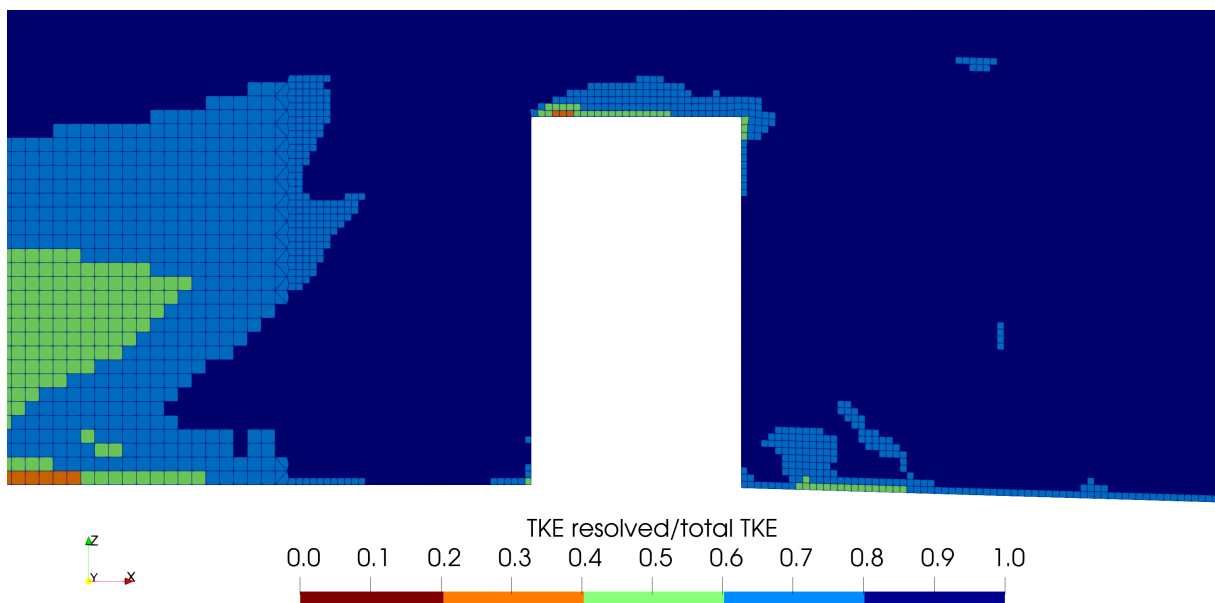


Figure C-1: Centerline cross-sections of (a) crossbars CR1-3 and (b) detail of CR1 in the LES model for Q_2 , showing the ratio of resolved to total turbulence kinetic energy (TKE) per cell, which should be greater than 0.8. In (a), the time-averaged water level is indicated by a thin, white, wavy line.

Appendix D

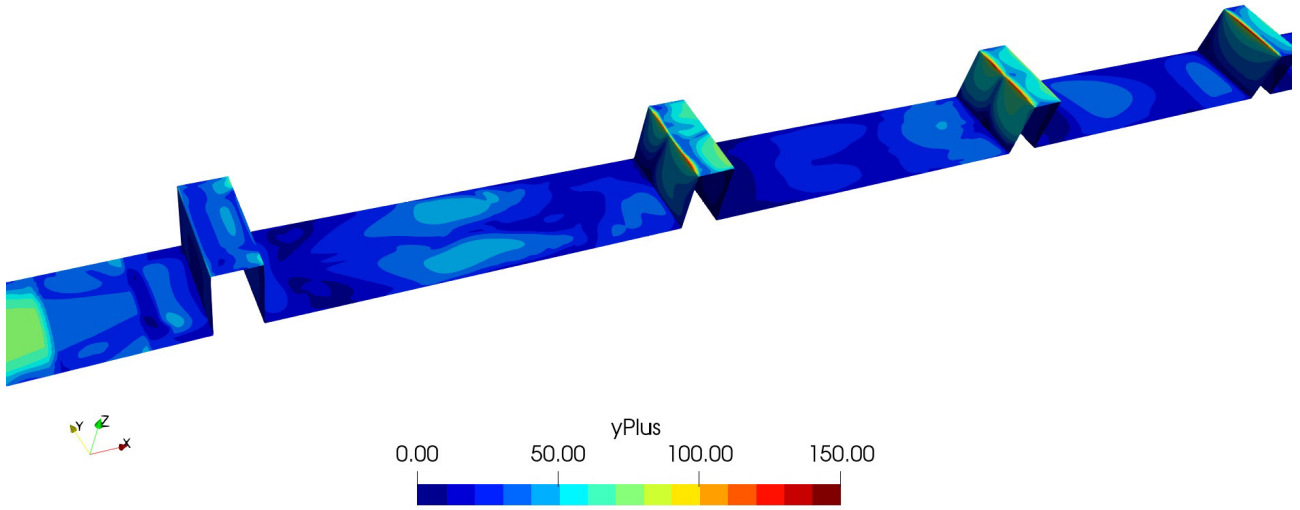


Figure D-1: Diagonal view of crossbars CR1-4 in the RANS model for Q_2 , showing values of $y^+ \approx 20-30$ at the pool and crossbar boundaries, and $y^+ \approx 130$ at the crossbar upstream edges. Flow direction from left to right.